Néel-type skyrmion lattice with confined orientation in the polar magnetic semiconductor GaV_4S_8

I. Kézsmárki[1,2]*, S. Bordács[1], P. Milde[3], E. Neuber[3], L. M. Eng[3], J. S. White[4], H. M. Rønnow[5], C. D. Dewhurst[6], M. Mochizuki[7,8], K. Yanai[7], H. Nakamura[9], D. Ehlers[2], V. Tsurkan[2,10] and A. Loidl[2]

Following the early prediction of the skyrmion lattice (SkL)—a periodic array of spin vortices—it has been observed recently in various magnetic crystals mostly with chiral structure. Although non-chiral but polar crystals with C_{nv} symmetry were identified as ideal SkL hosts in pioneering theoretical studies, this archetype of SkL has remained experimentally unexplored. Here, we report the discovery of a SkL in the polar magnetic semiconductor GaV_4S_8 with rhombohedral (C_{3v}) symmetry and easy axis anisotropy. The SkL exists over an unusually broad temperature range compared with other bulk crystals and the orientation of the vortices is not controlled by the external magnetic field, but instead confined to the magnetic easy axis. Supporting theory attributes these unique features to a new Néel-type of SkL describable as a superposition of spin cycloids in contrast to the Bloch-type SkL in chiral magnets described in terms of spin helices.

In non-centrosymmetric crystals, the energy associated with ferromagnetic domain walls can be negative; hence, the homogeneous ferromagnetic state becomes unstable against SkL formation[1–5]. Two basic types of magnetic domain walls can form various skyrmionic spin textures[1,3,4,6]. Bloch-type domain walls, where the spins rotate in the plane parallel to the domain boundary, can form, for example, whirlpool-like skyrmions. Such Bloch vortices have been observed in chiral magnets[7–19]. In contrast, Néel-type domain walls, with spins rotating in a plane perpendicular to the domain boundary, can produce vortices where the spins rotate in the radial planes from their cores to their peripheries. The magnetization patterns of such Bloch- and Néel-type skyrmions are illustrated in Fig. 1. The latter, expected to emerge in polar magnets with C_{nv} crystal symmetry[1,3,4,6], has not been observed yet in bulk crystals. We reveal the formation of such a Néel-type SkL in GaV_4S_8, a magnetic semiconductor from this crystal symmetry class, by means of magnetic susceptibility, atomic force microscopy (AFM) and small-angle neutron scattering (SANS) measurements.

GaV_4S_8, a member of the lacunar spinel family[20–27], has a non-centrosymmetric cubic (T_d) structure at room temperature[26]. Lacunar describes the lack of every second Ga atom compared to the normal spinel structure. These ordered defects break the vanadium pyrochlore lattice into a network of alternating larger and smaller V_4 tetrahedra, the so-called breathing pyrochlore lattice[28,29]. The magnetic building blocks are the smaller V_4 clusters with spin 1/2, and form a face-centred cubic (FCC) lattice. The hybridization on a single V_4 unit leads to one unpaired electron occupying a triply degenerate cluster orbital. This orbital degeneracy is lifted by a cooperative Jahn–Teller distortion that drives a cubic to rhombohedral structural transition at $T_s = 42$ K (refs 26,27). In the polar rhombohedral (C_{3v}) phase the FCC lattice is stretched along one of the four cubic ⟨111⟩ axes[26].

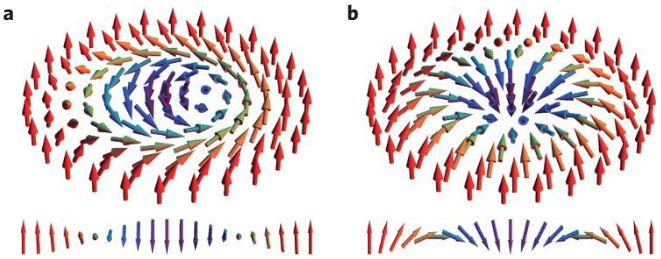

Figure 1 | Comparison between Bloch- and Néel-type skyrmions following refs 4,6. a, In a Bloch-type skyrmion, the spins rotate in the tangential planes—that is, perpendicular to the radial directions—when moving from the core to the periphery. **b**, In a Néel-type skyrmion, the spins rotate in the radial planes from the core to the periphery. The cross-section of the vortex is also depicted in both cases.

The structural transition creates a multi-domain state with submicron-thick sheets of the four different rhombohedral domains, as seen in Fig. 2a. At T_s the magnetic exchange interaction changes from antiferromagnetic to ferromagnetic and the material undergoes a magnetic transition at $T_C = 13$ K, a temperature very close to the Curie–Weiss temperature in the rhombohedral phase[30]. In the inset of Fig. 2b, the dependence of the magnetization curves

[1]Department of Physics, Budapest University of Technology and Economics and MTA-BME Lendület Magneto-optical Spectroscopy Research Group, 1111 Budapest, Hungary. [2]Experimental Physics V, Center for Electronic Correlations and Magnetism, University of Augsburg, 86135 Augsburg, Germany. [3]Institut für Angewandte Photophysik, TU Dresden, D-01069 Dresden, Germany. [4]Laboratory for Neutron Scattering and Imaging, Paul Scherrer Institut, CH-5232 Villigen, Switzerland. [5]Laboratory for Quantum Magnetism, École Polytechnique Fédérale de Lausanne, CH-1015 Lausanne, Switzerland. [6]Institut Laue-Langevin, 6 rue Jules Horowitz, 38042 Grenoble, France. [7]Department of Physics and Mathematics, Aoyama Gakuin University, Sagamihara, Kanagawa 229-8558, Japan. [8]PRESTO, Japan Science and Technology Agency, Kawaguchi, Saitama 332-0012, Japan. [9]Department of Materials Science and Engineering, Kyoto University, Kyoto 606-8501, Japan. [10]Institute of Applied Physics, Academy of Sciences of Moldova, MD 2028, Chisinau, Republica Moldova. *e-mail: kezsmark@mail.bme.hu

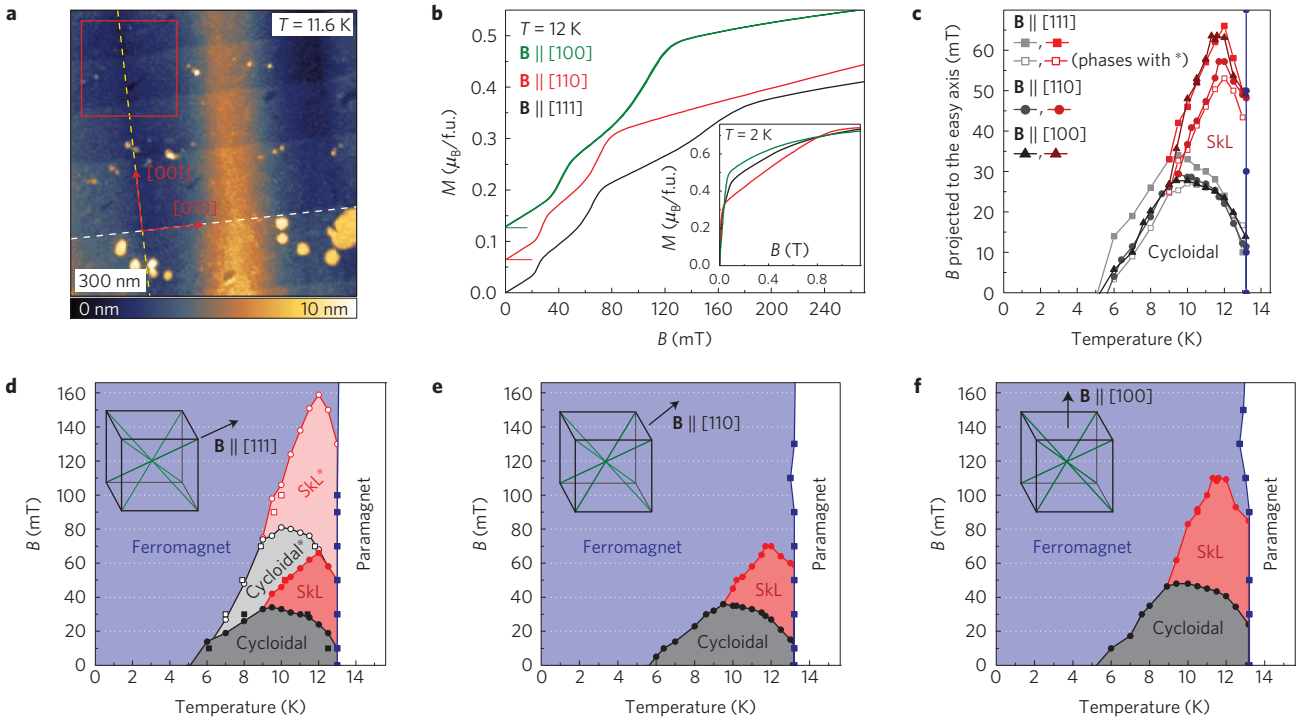

Figure 2 | Magnetic phases in the lacunar spinel GaV_4S_8. a, Topographic image recorded by AFM on the (100) surface of the crystal at $T = 11.6$ K. The colour scale corresponds to the altitude perpendicular to the image plane. Alternating blue and yellow stripes running along the cubic [001] direction are structural domains with different rhombohedral axes, whereas edges along the [010] axis are epilayer terraces. The yellow and white dashed lines highlight a domain boundary and a step between epilayer terraces, respectively. The magnetic patterns in Fig. 3 were recorded within the area of the red square. **b**, Magnetization curves measured at 12 K in **B** ∥ [100], [110] and [111] (shifted vertically for clarity). Magnetization steps are observed at different field values, depending on the orientation. The inset shows the magnetization measured at $T = 2$ K up to $B = 1.2$ T. **c**, Phase boundaries from **d**–**f**, after projecting the magnetic field onto the easy axis of the corresponding domains. **d**–**f**, Magnetic phase diagrams derived from the field- and the temperature dependence of the magnetization. Circles and squares correspond to peaks in the field- and temperature-derivative of the magnetization curves, respectively. The insets show the orientation of the magnetic field relative to the easy axes of the four rhombohedral domains (cubic body diagonals). The easy axes of magnetically favoured/unfavoured domains are indicated by thick/thin green lines. For **B** ∥ [111], besides the cycloidal and the SkL states, there are two additional phases extending up to higher fields, labelled as the cycloidal* and the SkL* states.

on the field orientation indicates a considerable anisotropy. Indeed, our mean-field analysis shows the ground state to be an easy axis ferromagnet with $J_{\parallel} \approx 4.35$ K and $J_{\perp} \approx 4.15$ K, as described in the Supplementary Information. Here, $J_{\parallel}$ and $J_{\perp}$ respectively denote the exchange coupling for spin components parallel and perpendicular to the easy axis, which itself coincides with the direction of the rhombohedral distortion. These exchange values are also consistent with $T_C = 13$ K.

GaV_4S_8 was considered as an ordinary ferromagnet below T_C (refs 26,30), although there is a report about low-field magnetic anomalies in this material[31]. We found that the magnetic state is far from ordinary, and contains several neighbouring phases. Below T_C, the low-field magnetization exhibits a sequence of steps indicating metamagnetic transitions (see Fig. 2b). The positions of the steps, associated with sharp peaks in the field-derivative of the magnetization, are different for the magnetic field, **B**, applied parallel to the [111], [110] and [100] cubic axes. The corresponding phase diagrams are shown in Fig. 2d–f. Similar low-field steps have been observed to separate the helical, SkL and conical states in MnSi (refs 7,18,32,33), $Mn_{1-x}(Co,Fe)_xSi$ (ref. 34), FeGe (ref. 11) and Cu_2OSeO_3 (ref. 12). In GaV_4S_8 we assign the three different magnetic phases as cycloidal, Néel-type SkL and ferromagnetic, on the basis of AFM imaging, SANS experiments and theoretical calculations, as described below. This assignment is in accord with the results of pioneering works predicting the emergence of the cycloidal and Néel-type SkL states in materials belonging to the C_{nv} symmetry class[1–4].

For **B** ∥ [111] there exist two additional magnetic states besides the cycloidal, SkL and ferromagnetic states. This arises due to the multi-domain nature of the crystal and the easy axis anisotropy, as only one of the domains has its easy axis parallel to **B**, whereas the easy axes of the other three domains—$[11\bar{1}]$, $[1\bar{1}1]$ and $[\bar{1}11]$—lie at 71° to **B**. For these latter three domains the non-collinear spin structures survive to higher fields because the magnetic anisotropy energy is much larger than the Zeeman energy, and only the field component parallel to the easy axis of each domain can influence its magnetic state. This leads to the two additional phases persisting up to $B = 80$ mT and 160 mT, marked with asterisks in Fig. 2d, and assigned as the cycloidal and SkL states common for these three domains. For **B** ∥ [110], the cycloidal and SkL phases common for the two domains with easy axes [111] and $[11\bar{1}]$ are indicated in Fig. 2e. The other two domains with easy axes perpendicular to **B** cannot contribute to the magnetization in this field range. For **B** ∥ [100], the easy axis of each domain makes the same angle with **B**, hence all domains share common phase boundaries, as shown in Fig. 2f. Phase boundaries for all field orientations can be scaled together by projecting the field onto the easy axes of the corresponding domains (see Fig. 2c). Surprisingly, the SkL state exists over an unusually broad temperature range, down to $\sim 0.68 T_C$, compared with other bulk crystals, where the stability of this phase is limited to the temperature range $0.9 T_C \leq T \leq T_C$ (refs 7,10,12).

To observe directly the spin pattern in real space we performed non-contact AFM imaging in magnetic fields applied perpendicular to the sample surface using magnetic cantilever tips (for technical

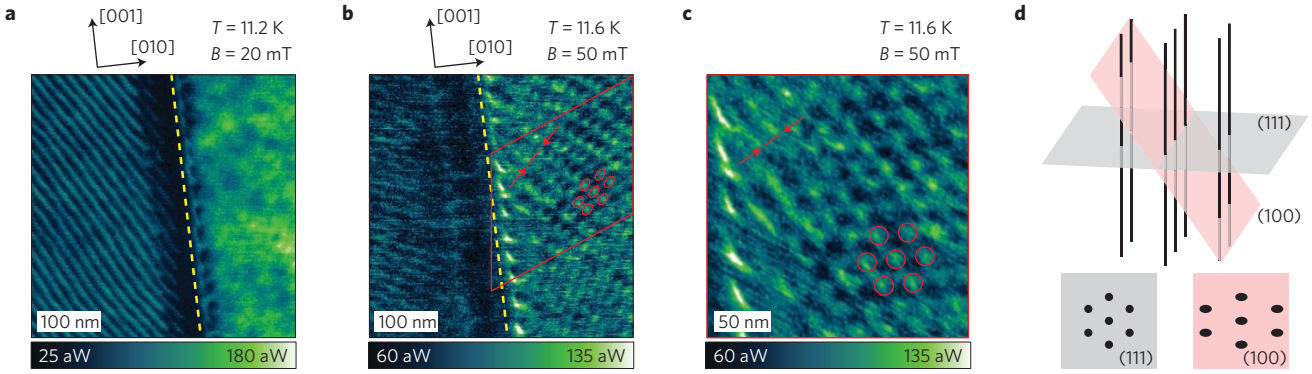

Figure 3 | Real-space imaging of the magnetic patterns in GaV_4S_8. a, AFM image recorded at $T = 11.2$ K and in $B = 20$ mT on the (100) surface in the area indicated by the red square in Fig. 2a. Colour coding corresponds to the dissipated power due to magnetic interactions between the tip and the sample. A modulated structure with a single **q**-vector and a corresponding periodicity of $a_{cyc} = 17.7 \pm 0.4$ nm is observed on the left side of the domain boundary (yellow dashed line). The weak magnetic contrast does not allow the determination of the magnetic pattern on the other domain. **b**, Magnetic pattern measured in the same area at $T = 11.6$ K and in $B = 50$ mT. A distorted triangular lattice is observed on the right side of the domain boundary. (See the Supplementary Information for similar images taken at different temperatures and magnetic fields.) The area with red border is scaled by $\sqrt{3}$ according to the red arrows—that is, perpendicular to the direction of the shortest lattice periodicity. The area, transformed to a square shape after this contraction, is shown in **c**. **c**, The green spots indicate a regular triangular SkL with a lattice constant of $a_{sky} = 22.2 \pm 1$ nm and vortex cores parallel to the [111] axis. For more details about the data analysis and the evolution of the magnetic pattern as a function of magnetic field, see the Supplementary Information. **d**, Two sections of a hexagonal array of vortex lines running along the [111] axis. The intersections of the vortices with the (111) and (100) planes form a regular and a distorted triangular lattice, respectively.

details see the Methods)[15]. For $\mathbf{B} \parallel [100]$, Fig. 3a,b shows images of the same surface area taken at $T = 11.2$ K and 11.6 K in magnetic fields $B = 20$ mT and 50 mT, respectively. The trail running along the [001] axis and dividing each image into two halves is a structural domain boundary.

Although all four domains should host the same magnetic states for $\mathbf{B} \parallel [100]$, we found that the magnetic pattern always changed at the domain boundaries, and often it was not possible to achieve good contrast for the two sides simultaneously. As the wavevectors of the magnetic modulation (**q**-vector) are expected to be perpendicular to the easy axis, they can be different for different domains, resulting in a rotation of the magnetic pattern between the two sides. In Fig. 3a, a modulated structure with a single **q**-vector, representative of the zero- and low-field region, is observed with good contrast on the left side. Our calculations described later reproduce this phase as a cycloidal spin state, where the spins rotate in a plane containing the **q**-vector. This is in contrast to the helical order generally found in other SkL materials, where the spins rotate in the plane perpendicular to **q**. Assuming that the **q**-vector is perpendicular to the easy axis, which is either the $[11\bar{1}]$ or $[1\bar{1}1]$ axis for the left-side domain, the periodicity of the cycloid in $B = 20$ mT is $a_{cyc} = 17.7 \pm 0.4$ nm. (For more details see the Supplementary Information.) This value is confirmed by our SANS study.

With increasing field the cycloidal pattern disappears and a distorted triangular lattice emerges with sufficient contrast on the right side of the domain wall in Fig. 3b. As demonstrated in Fig. 3c, re-scaling the lattice on the right side by $\sqrt{3}$ perpendicular to the direction of the shortest lattice constant leads to a regular triangular lattice with a lattice constant of $a_{sky} = 22.2 \pm 1$ nm. This value is also consistent with our SANS data. The observed distortion is naturally explained by the orientational confinement of the SkL. As the vortex cores are not aligned parallel to the magnetic field, but instead the easy axis, which is either the [111] or $[\bar{1}11]$ axis for the right-side domain, they form a regular triangular lattice in the hard plane. Therefore, the terminus of the vortices on the (100) surface forms a distorted triangular lattice, as sketched in Fig. 3d. When further increasing the field, the magnetic pattern disappears, indicating a uniform ferromagnetic state.

SANS was employed to confirm the bulk nature of the magnetic structures and determine the **q**-vectors directly[7,35]. Magnetic Bragg spots were always observed with **q**-vectors parallel to the cubic $\langle 1\bar{1}0 \rangle$ directions, irrespective of the field orientation, as shown in Fig. 4. As the cycloidal or SkL states in each rhombohedral domain exhibit three $\langle 1\bar{1}0 \rangle$ **q**-vectors, the SANS diffraction spots can have overlapping contributions from **q**-vectors in different domains. For $\mathbf{B} \parallel [111]$ the **q**-vectors form a regular hexagon. Here, scattering from the unique domain with easy axis parallel to the field contributes to all six spots (each of the three **q**-vectors gives scattering at $\pm\mathbf{q}$). From the three other domains, only a single **q**-vector satisfies the Bragg condition, and the scattering from each overlaps with spots arising from the unique domain. For $\mathbf{B} \parallel [100]$, a square pattern of four spots is observed. Here single **q**-vectors in two of the domains contribute to either the vertical or horizontal spot pairs, with the Bragg condition not fulfilled for the other **q**-vectors.

These results, in agreement with AFM imaging, confirm the orientational confinement of the SkL—that is, the alignment of the vortex lines parallel to the easy axis of each domain. It also shows that, in both the cycloidal and SkL states, the three possible **q** vectors are parallel to the three $\langle 1\bar{1}0 \rangle$ axes lying in the hard plane. For $\mathbf{B} \parallel [111]$ a pale ring structure appears besides the hexagon in low fields. This implies that the **q**-vectors are not fully pinned to the $\langle 1\bar{1}0 \rangle$ axes but can point in any direction within the hard plane, at least in the surface and domain boundary regions observed by AFM.

In each rhombohedral domain the cycloidal state can emerge with three different **q**-vectors, whereas the SkL state is unique, and describable as a superposition of three cycloids whose **q**-vectors sum to zero. First-order Bragg peaks observed using SANS do not allow a direct distinction between the cycloidal and the SkL states owing to the presence of magnetic and structural domains. Nevertheless, for $\mathbf{B} \parallel [100]$, when all four structural domains are magnetically equivalent, the field dependence of the total Bragg intensity evidences both the cycloidal to SkL and the SkL to ferromagnetic transitions (see Fig. 5d). For $\mathbf{B} \parallel [111]$, the magnetization data in Fig. 2d imply that the cycloidal and SkL phases in the unique domain, with easy axis parallel to the field, exist in lower fields compared to the other three domains. To confirm this scenario, we analysed the angular dependence of the SANS intensity (the so-called rocking curve) with $\mathbf{q} \parallel [01\bar{1}]$—that is, for the upper peak in the images of Fig. 4a–c. As shown in Fig. 5a, the rocking curve includes both a central peak and a flat part extending beyond

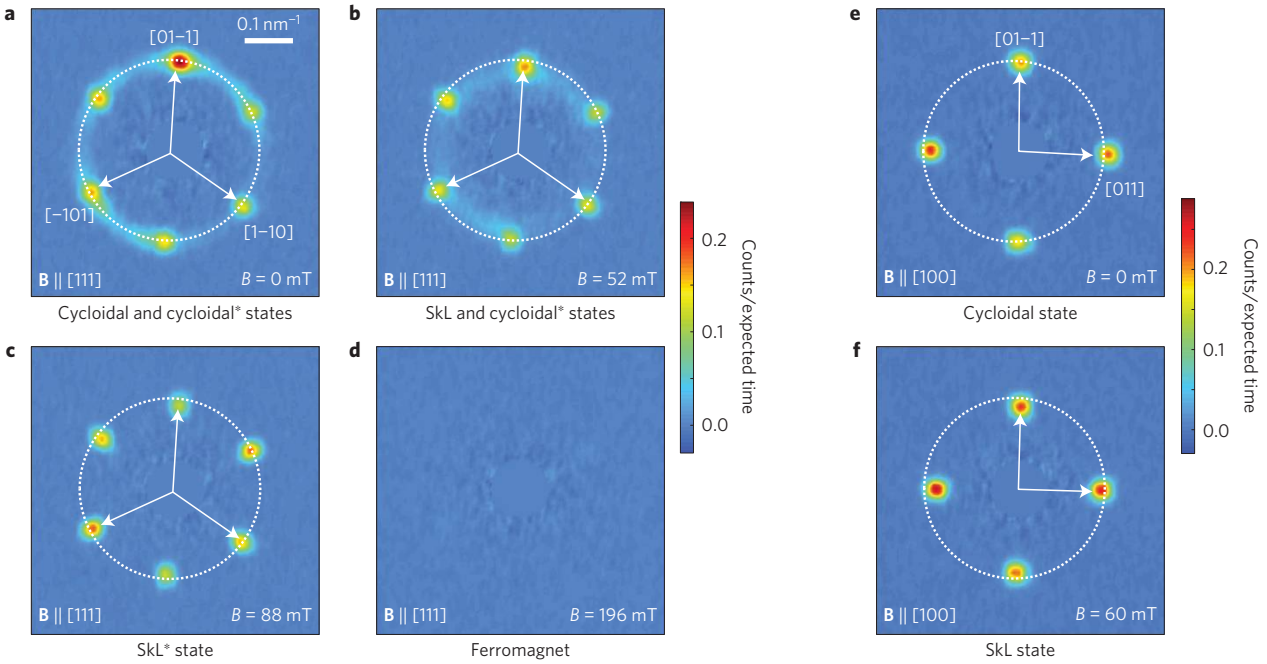

Figure 4 | Small-angle neutron scattering study of the magnetic states in GaV_4S_8. a–d, SANS images measured at $T = 10.9$ K in various fields for **B** ∥ [111]. The images were recorded at field values representative of the different magnetic states assigned in Fig. 2d. **e**,**f**, SANS images taken at $T = 10.9$ K in different magnetic fields for **B** ∥ [100]. Labels refer to the magnetic states assigned in Fig. 2f. The dashed circles having common diameter in all the images help in visualizing the change in the magnitude of the **q**-vectors. The two colour bars indicate the scattering intensity for the two field orientations.

the measured angular range. The central peak is due to magnetic scattering from the unique domain: its intensity is fully suppressed when the SkL phase vanishes, and it also shows an anomaly at the cycloidal to SkL transition (see Fig. 5c). The flat part, vanishing only at the SkL* to ferromagnetic transition, represents scattering from the other domains.

The origin of the different contributions to the SANS intensity deduced from the rocking curves is also confirmed by the $|\mathbf{q}|$-dependence of the intensity. As shown in Fig. 5b, for SANS images recorded in the central region of the rocking curve, a double-peak structure is observed, whereas only the peak at higher $|\mathbf{q}|$ appears for images taken in the flat part of the rocking curve. Moreover, the peak at lower $|\mathbf{q}|$ disappears entirely at $B = 60$ mT, where the SkL to ferromagnetic transition takes place in the unique domain. As shown in Fig. 5c, from this analysis we could distinguish the periodicities ($a = 2\pi/|\mathbf{q}|$) of the magnetic structures in the two types of domains.

As indicated in Fig. 5b, all individually resolved Bragg peaks are resolution-limited within the detector plane, which hinders the determination of the magnetic correlation lengths. On the other hand, the out-of-plane correlations probed by the rocking curve width are not limited by the instrumental resolution, and we could estimate the correlation length along and perpendicular to the skyrmion cores as ∼540 nm and ∼110 nm, respectively (for more details see Methods). Concerning our AFM studies, the typical thickness of the sheet-like structural domains varies in the range ∼200–700 nm. Correspondingly, the domain size of the SkL is limited by the size of the underlying structural domains along the skyrmion cores, but not in the perpendicular directions.

In GaV_4S_8, the $S = 1/2$ spins sit on an FCC lattice stretched along the [111] direction, which can be regarded as triangular lattices stacked along [111]. To determine the spin patterns in the different phases we studied the following classical Heisenberg model on the triangular lattice by a Monte Carlo technique;

$$\mathcal{H} = \mathcal{H}_{ex} + \mathcal{H}_{DM} + \mathcal{H}_{Zeeman} \quad (1)$$

where

$$\mathcal{H}_{ex} = -\sum_{\langle i,j \rangle} \left(J_\perp m_{xi} m_{xj} + J_\perp m_{yi} m_{yj} + J_\parallel m_{zi} m_{zj} \right)$$

$$\mathcal{H}_{DM} = \sum_{\langle i,j \rangle} \mathbf{D}_{ij} (\mathbf{m}_i \times \mathbf{m}_j)$$

$$\mathcal{H}_{Zeeman} = -B \sum_i m_{zi}$$

For the exchange interaction $\mathcal{H}_{ex}$, we consider ferromagnetic coupling with XXZ-type anisotropy between the local magnetic moment $\mathbf{m}_i$ of neighbouring V_4 clusters, where the z (easy) axis is parallel to [111]. The direction of the Dzyaloshinskii–Moriya vectors, $\mathbf{D}_{ij}$, are determined by the FCC crystal symmetry, as shown in Fig. 6a. For the calculation we choose realistic exchange parameters for GaV_4S_8: $J_\parallel/J_\perp = 1.08$ determined from the mean-field analysis of the magnetization curves and $D/J_\perp = 0.35$ fixed according to the observed cycloidal pitch, where $D = |\mathbf{D}_{ij}|$.

This model provides three ordered phases with increasing strength of the magnetic field: the cycloidal, SkL and ferromagnetic state. Figure 6 shows the spin patterns obtained for the cycloidal and SkL state. The skyrmions exhibit the Néel-type domain wall alignment along the radial direction from their cores to their peripheries. Namely, the spins rotate within the plane parallel to the radial direction. We stress that, irrespective of the details of possible models, GaV_4S_8 can host only a Néel-type SkL owing to the orientation of Dzyaloshinskii–Moriya vectors characteristic to the C_{nv} symmetry class[1–4,6]. This statement is further supported by our calculations on a lattice model with C_{4v} symmetry. This calculation can reproduce the experimental phase diagram in Fig. 2c as well as the field dependence of the SANS intensity on a semiquantitative level (see the Supplementary Information). For the triangular lattice model, the Fourier components of the magnetization configurations in the cycloidal and the SkL states are shown in Fig. 6d,g, respectively. These results, in full agreement with

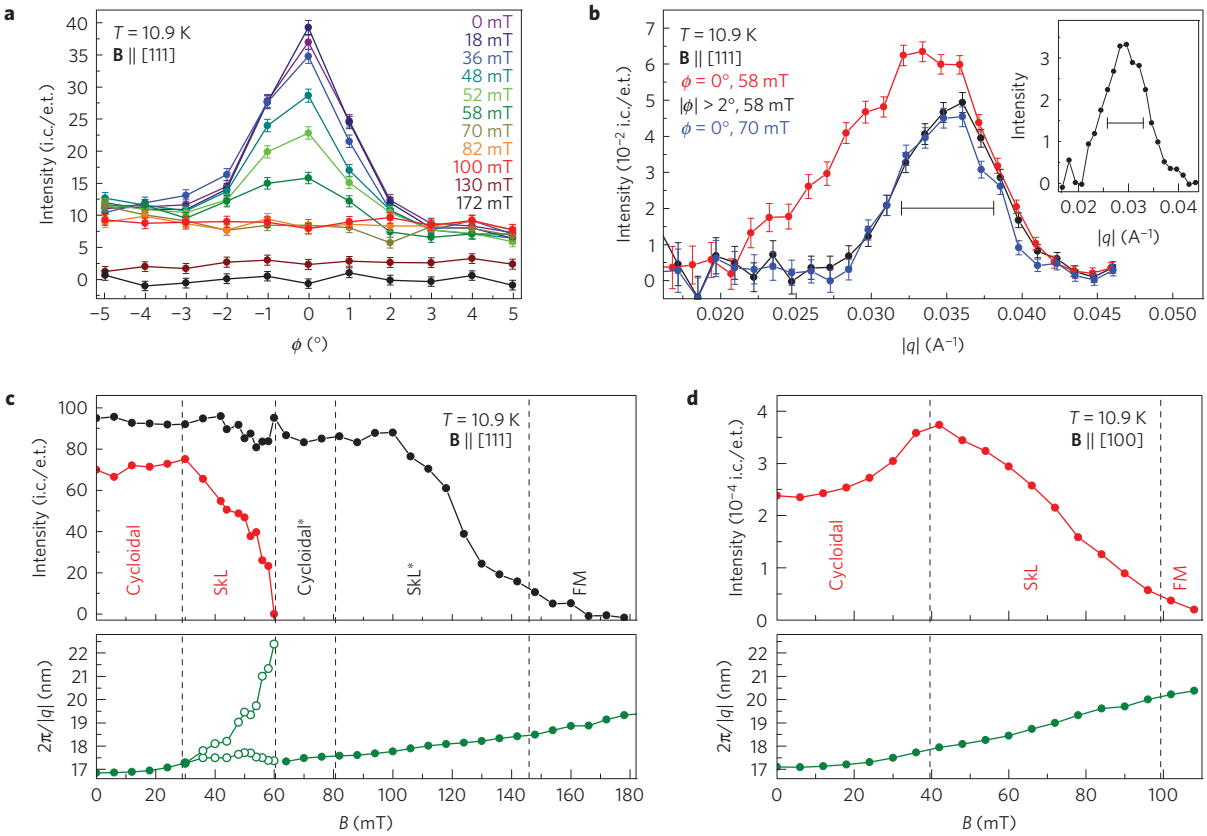

Figure 5 | Tracing the magnetic phase boundaries by SANS. a, Angular dependence of the SANS intensity in various magnetic fields. The sample is rotated together with the magnetic field by an angle ϕ around the horizontal axis (orthogonal to both the scattering vector $\mathbf{q} \parallel [01\bar{1}]$ and the incoming beam). The rocking curves, representing the angular dependence of the total intensity of the $\mathbf{q} \parallel [01\bar{1}]$ Bragg spot, are characterized by a central peak located between ±2° and a flat part. Error bars are determined by assuming Poissonian statistics. **b**, $|\mathbf{q}|$-dependence of the SANS intensity along $[01\bar{1}]$ in $B = 58$ mT measured at rotation angles in the central region (red line) and the flat part (black line) of the corresponding rocking curve. The inset shows the difference between the red and black curves. The blue curve is representative of fields larger than $B = 60$ mT, for which the $|\mathbf{q}|$-dependence of the intensity is uniform for all angles between ±5°. Horizontal bars indicate the instrumental resolution. **c**,**d**, The scattering intensity (upper part) and the magnetic periodicity, $a = 2\pi/|\mathbf{q}|$, (lower part) as a function of field for the two magnetic field orientations. Vertical dashed lines indicate the phase boundaries according to Fig. 2d,f. For $\mathbf{B} \parallel [100]$, the total scattering intensity summed over the Bragg spots is shown. For $\mathbf{B} \parallel [111]$, the intensity of the $[01\bar{1}]$ Bragg spot is plotted for the central region (red line) and the flat part (black line) of the rocking curve. As exemplified in **b** for $B = 58$ mT, the splitting of the Bragg spot into two peaks with different $|\mathbf{q}|$ was resolved in the field range $B = 30$–60 mT, which arises from the coexistence of cycloidal* and SkL states in different rhombohedral domains. This splitting is emphasized by using open symbols over the corresponding field range.

SANS data, show that the **q**-vectors are parallel to the $\langle 1\bar{1}0 \rangle$ axes in the hard plane in both states. In cubic helimagnets the orientation of the **q**-vectors is defined by the weak magnetocrystalline anisotropy[36,37]. In contrast, we found that in GaV_4S_8 the orientation of Dzyaloshinskii–Moriya vectors alone determines the direction of the **q**-vectors, without additional magnetic anisotropies in the hard plane—that is, perpendicular to the vortex cores. The lack of a conical spin state, which is generally present in the phase diagram of cubic helimagnets, is also reproduced by these calculations, in agreement with previous theoretical works[1,6,38].

Recent experimental and theoretical studies[18,19] on cubic helimagnet films with uniaxial distortion have revealed SkL phases existing over broad temperature regions similar to GaV_4S_8. Whereas the pattern of the Dzyaloshinskii–Moriya vectors on the crystal lattice and the magnetic structure of the skyrmions are different in the two cases, the key role of finite axial anisotropy in stabilizing the SkL phase against the conical state seems to be universal, as already predicted in early studies[1–4]. In the case of thin films the uniaxial anisotropy is determined by the substrate and the film thickness. In GaV_4S_8, the application of pressure can be an efficient tool to tune the strength of uniaxial anisotropy, and thus address its role in the formation and stability of the SkL phase.

In a new class of materials we observed a SkL state emerging over an extraordinarily broad temperature range. Although Bloch-type skyrmions have been investigated extensively in chiral magnets, lacunar spinels provide a unique arena to study another topological spin pattern, the Néel-type skyrmions. We found that the strong orientational confinement of the vortices ensures the robustness of two distinct skyrmionic states with a core magnetization pointing either up or down the easy axis. This may facilitate a unique magnetic control of the SkL, as we expect that the SkL induced by a magnetic field parallel to the easy axis can be rotated within the hard plane by an additional transverse field component. Such magnetic control is inconceivable in cubic helimagnets where vortex cores instantaneously co-align with the magnetic field. In addition, the polar crystal structure of lacunar spinels[25–27] may be exploited for a non-dissipative electric field control of the SkL. Recent studies have successfully demonstrated the creation, manipulation and atomic-scale magnetic profiling of individual skyrmions[16,39–41], which are the basic functions required for a novel type of information technology built on skyrmion-based memory devices[40,42–44]. The magnetic and/or electric control of skyrmions can play a crucial role in the technological realization of such devices.

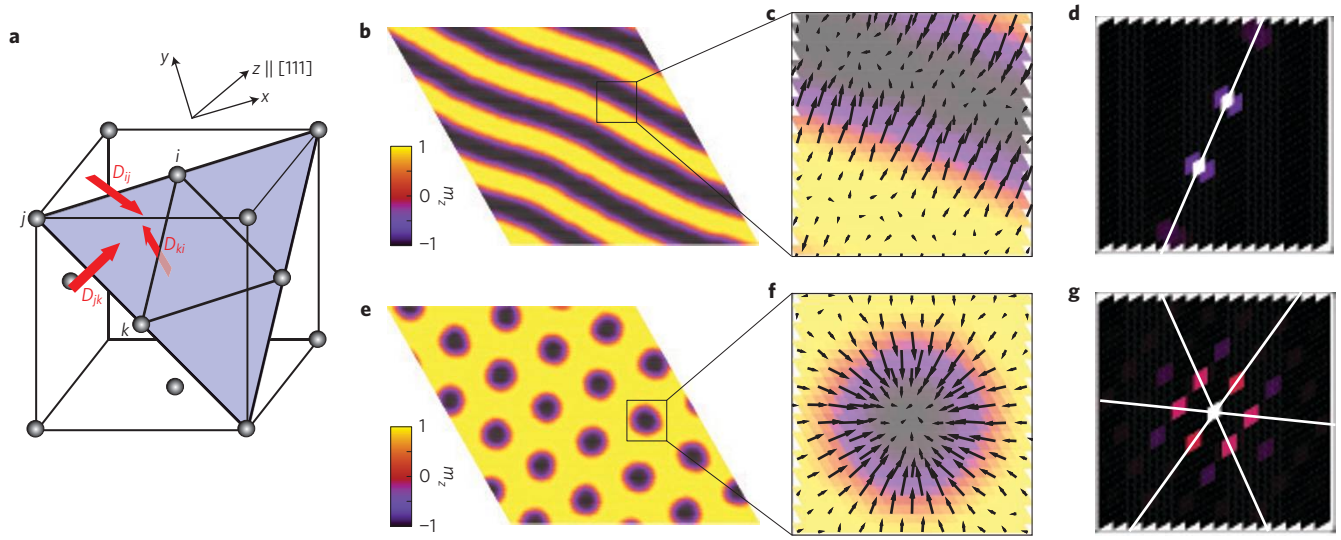

Figure 6 | Spin patterns in the magnetic phases of GaV_4S_8. a, FCC lattice of V_4 units, each carrying a spin 1/2, and the orientation of the Dzyaloshinskii–Moriya vectors for bonds on the triangular lattice within the (111) plane (chosen as the *xy* plane in the calculation). **b**, Cycloidal spin state obtained for the spin model in equation (1) on the triangular lattice in zero magnetic field. The colour coding indicates the out-of-plane components of the spins. **c**, Magnified view of the magnetization configuration for the cycloidal state. The arrows correspond to the in-plane components of the spins at every second site of the triangular lattice. (The remainder of the sites are not shown to reduce the density of the arrows and preserve the clarity of the figure.) **d**, Bragg peaks (**q**-vectors) of the cycloidal state in **b** in reciprocal space. **e**, SkL state obtained for the spin model in equation (1) on the triangular lattice for $B/J_\perp = 0.08$ along the *z* axis. The colour coding is the same as in **b**. **f**, Magnified view of the magnetization configuration for the SkL state clearly shows the Néel-type domain wall alignment. Note that the magnetization points opposite to the magnetic field in the core region of the skyrmions. (Similarly to **c**, only every second spin is shown.) **g**, Bragg peaks of the SkL state in **e**. The **q**-vectors of first-order Bragg peaks are located along the $\langle 1\bar{1}0 \rangle$ directions (white lines) in the hard plane, for both the cycloidal and SkL states.

Methods

Methods and any associated references are available in the online version of the paper.

References

1. Bogdanov, A. N. & Yablonskii, D. A. Thermodynamically stable 'vortices' in magnetically ordered crystals. The mixed state of magnets. *Zh. Eksp. Teor. Fiz.* **95,** 178–182 (1989).
2. Bogdanov, A. N. & Yablonskii, D. A. Contribution to the theory of inhomogeneous states of magnets in the region of magnetic-field-induced phase transitions. Mixed state of antiferromagnets. *Zh. Eksp. Teor. Fiz.* **96,** 253–260 (1989).
3. Bogdanov, A. N. & Hubert, A. Thermodynamically stable magnetic vortex states in magnetic crystals. *J. Magn. Magn. Mater.* **138,** 255–269 (1994).
4. Bogdanov, A. N. & Hubert, A. The properties of isolated magnetic vortices. *Phys. Status Solidi b* **186,** 527–543 (1994).
5. Rössler, U. K., Bogdanov, A. N. & Pfleiderer, C. Spontaneous skyrmion ground states in magnetic metals. *Nature* **422,** 797–801 (2006).
6. Leonov, A. *Twisted, Localized, and Modulated States Described in the Phenomenological Theory of Chiral and Nanoscale Ferromagnets* PhD thesis (2014); http://nbn-resolving.de/urn:nbn:de:bsz:14-qucosa-83823
7. Mühlbauer, S. *et al.* Skyrmion lattice in a chiral magnet. *Science* **323,** 915–919 (2009).
8. Münzer, W. *et al.* Skyrmion lattice in the doped semiconductor $Fe_{1-x}Co_xSi$. *Phys. Rev. B* **81,** 041203(R) (2010).
9. Yu, X. Z. *et al.* Real-space observation of a two-dimensional skyrmion crystal. *Nature* **465,** 901–904 (2010).
10. Yu, X. Z. *et al.* Near room-temperature formation of a skyrmion crystal in thin-films of the helimagnet FeGe. *Nature Mater.* **10,** 106–109 (2011).
11. Wilhelm, H. *et al.* Precursor phenomena at the magnetic ordering of the cubic helimagnet FeGe. *Phys. Rev. Lett.* **107,** 127203 (2011).
12. Seki, S., Yu, X. Z., Ishiwata, S. & Tokura, Y. Observation of skyrmions in a multiferroic material. *Science* **336,** 198–201 (2012).
13. Adams, T. *et al.* Long-wavelength helimagnetic order and skyrmion lattice phase in Cu_2OSeO_3. *Phys. Rev. Lett.* **108,** 237204 (2012).
14. Tonomura, A. *et al.* Real-space observation of skyrmion lattice in helimagnet MnSi thin samples. *Nano Lett.* **12,** 1673–1677 (2012).
15. Milde, P. *et al.* Unwinding of a skyrmion lattice by magnetic monopoles. *Science* **340,** 1076–1080 (2013).
16. Shibata, K. *et al.* Towards control of the size and helicity of skyrmions in helimagnetic alloys by spin–orbit coupling. *Nature Nanotech.* **8,** 723–728 (2013).
17. Park, H. S. *et al.* Observation of the magnetic flux and three dimensional structure of skyrmion lattices by electron holography. *Nature Nanotech.* **9,** 337–342 (2014).
18. Wilson, M. N. *et al.* Extended elliptic skyrmion gratings in epitaxial MnSi thin films. *Phys. Rev. B* **86,** 144420 (2012).
19. Wilson, M. N. *et al.* Chiral skyrmions in cubic helimagnet films: The role of uniaxial anisotropy. *Phys. Rev. B* **89,** 094411 (2014).
20. Ta Phouc, V. *et al.* Optical conductivity measurements of $GaTa_4Se_8$ under high pressure: Evidence of a bandwidth-controlled insulator-to-metal Mott transition. *Phys. Rev. Lett.* **110,** 037401 (2013).
21. Abd-Elmeguid, M. M. *et al.* Transition from Mott insulator to superconductor in $GaNb_4Se_8$ and $GaTa_4Se_8$ under high pressure. *Phys. Rev. Lett.* **93,** 126403 (2004).
22. Dorolti, E. *et al.* Half-metallic ferromagnetism and large negative magnetoresistance in the new lacunar spinel $GaTi_3VS_8$. *J. Am. Chem. Soc.* **132,** 5704–5710 (2010).
23. Kim, H.-S., Im, J., Han, M. J. & Jin, H. Spin-orbital entangled molecular $j_{\rm eff}$ states in lacunar spinel compounds. *Nature Commun.* **5,** 3988 (2014).
24. Guiot, V. *et al.* Avalanche breakdown in $GaTa_4Se_{8-x}Te_x$ narrow-gap Mott insulators. *Nature Commun.* **4,** 1722 (2013).
25. Singh, K. *et al.* Orbital-ordering-driven multiferroicity and magnetoelectric coupling in GeV_4S_8. *Phys. Rev. Lett.* **113,** 137602 (2014).
26. Pocha, R., Johrendt, D. & Pöttgen, R. Electronic and structural instabilities in GaV_4S_8 and $GaMo_4S_8$. *Chem. Mater.* **12,** 2882–2887 (2000).
27. Ruff, E. *et al.* Ferroelectric skyrmions and a zoo of multiferroic phases in GaV_4S_8. Preprint at http://xxx.lanl.gov/abs/1504.00309 (2015).
28. Okamoto, Y., Nilsen, G. J., Attfield, J. P. & Hiroi, Z. Breathing pyrochlore lattice realized in A-site ordered spinel oxides $LiGaCr_4O_8$ and $LiInCr_4O_8$. *Phys. Rev. Lett.* **110,** 097203 (2013).
29. Kimura, K., Nakatsuji, S. & Kimura, T. Experimental realization of a quantum breathing pyrochlore antiferromagnet. *Phys. Rev. B* **90,** 060414(R) (2014).
30. Yadav, C. S., Nigam, A. K. & Rastogi, A. K. Thermodynamic properties of ferromagnetic Mott-insulator GaV_4S_8. *Physica B* **403,** 1474–1475 (2008).

31. Nakamura, H. *et al.* Low-field multi-step magnetization of GaV_4S_8 single crystal. *J. Phys. Conf. Ser.* **145,** 012077 (2009).
32. Thessieu, C., Pfleiderer, C., Stepanov, A. N. & Flouquet, J. Field dependence of the magnetic quantum phase transition in MnSi. *J. Phys. Condens. Matter* **9,** 6677–6687 (1997).
33. Lamago, D., Georgii, R., Pfleiderer, C. & Böni, P. Magnetic-field induced instability surrounding the A-phase of MnSi: Bulk and SANS measurements. *Physica B* **385–386,** 385–387 (2006).
34. Pfleiderer, C. *et al.* Skyrmion lattices in metallic and semiconducting B_20 transition metal compounds. *J. Phys. Condens. Matter* **22,** 164207 (2010).
35. Adams, T. *et al.* Long-range crystalline nature of the skyrmion lattice in MnSi. *Phys. Rev. Lett.* **107,** 217206 (2011).
36. Bak, P. & Jensen, M. H. Theory of helical magnetic structures and phase transitions in MnSi and FeGe. *J. Phys. C: Solid State Phys.* **13,** L881–L885 (1980).
37. White, J. S. *et al.* Electric-field-induced skyrmion distortion and giant lattice rotation in the magnetoelectric insulator Cu_2OSeO_3. *Phys. Rev. Lett.* **113,** 107203 (2014).
38. Dzyloshinskii, I. E. Theory of helicoidal structures in antiferromagnets. I. Nonmetals. *Sov. Phys. JETP* **19,** 960–971 (1964).
39. Heinze, S. *et al.* Spontaneous atomic-scale magnetic skyrmion lattice in two dimensions. *Nature Phys.* **7,** 713–718 (2011).
40. Romming, N. *et al.* Writing and deleting single magnetic skyrmions. *Science* **341,** 636–639 (2013).
41. Romming, N., Kubetzka, A., Hanneken, C., von Bergmann, K. & Wiesendanger, R. Field-dependent size and shape of single magnetic skyrmions. *Phys. Rev. Lett.* **114,** 177203 (2015).
42. Fert, A., Cros, V. & Sampaio, J. Skyrmions on the track. *Nature Nanotech.* **8,** 152–156 (2013).
43. Sampaio, J., Cros, V., Rohart, S., Thiaville, A. & Fert, A. Nucleation, stability and current-induced motion of isolated magnetic skyrmions in nanostructures. *Nature Nanotech.* **8,** 839–844 (2013).
44. Mochizuki, M. *et al.* Thermally driven ratchet motion of a skyrmion microcrystal and topological magnon Hall effect. *Nature Mater.* **13,** 241–246 (2014).

Acknowledgements

We thank H. A. K. V. Nidda and T. Fehér for useful discussions. This work was supported by the Hungarian Research Funds OTKA K 108918, OTKA PD 111756 and Bolyai 00565/14/11, by the European Research Council Project CONQUEST, by the Swiss NSF Grant Nos. 153451, 146870 and 141962, by the DFG under Grant No. SFB 1143 and via the Transregional Research Collaboration TRR 80 From Electronic Correlations to Functionality (Augsburg/Munich/Stuttgart) and by JSPS KAKENHI under Grant Nos. 25870169 and 25287088 from MEXT Japan.

Author contributions

I.K., S.B., P.M., E.N., L.M.E., J.S.W., C.D.D., D.E. and V.T. performed the measurements; I.K., S.B., P.M., E.N., H.M.R., J.S.W. and A.L. analysed the data; V.T. and H.N. contributed to the sample preparation; M.M. and K.Y. developed the theory; I.K. wrote the manuscript and planned the project.

Competing financial interests

The authors declare no competing financial interests.

Methods

Sample synthesis and characterization. Single crystals of GaV_4S_8 were grown by the chemical vapour transport method using iodine as the transport agent. The crystals are typically cuboids or hexagonal slabs, with masses ranging from 1–60 mg. The sample quality was checked by powder X-ray diffraction, specific heat and magnetization measurements. The crystallographic orientation of the samples was determined by X-ray Laue and/or neutron diffraction before the magnetization, SANS and AFM studies. The magnetization measurements were performed using a magnetic property measurement system (MPMS) from Quantum Design. The field dependence of the magnetization was measured in increasing temperature steps following an initial zero-field cooling to 2 K. The temperature dependence of the magnetization was also measured in different fields. For both of these approaches, we found no hysteresis in the magnetization curves, thus indicating that the SkL state cannot be quenched—that is, stabilized as a metastable state—in this compound.

Non-contact atomic force microscopy. All AFM data presented were obtained by non-contact atomic force microscopy (nc-AFM) performed in an Omicron cryogenic ultrahigh vacuum (UHV) STM/AFM instrument using the RHK R9-control electronics. The microscope features interferometric detection, which as a side effect allows the tuning of the cantilevers' effective quality factor Q_{eff} by varying the laser intensity used for the detection of the cantilever motion. For all measurements we used magnetically coated AFM-tips from the SSS-QMFMR series from NANOSENSORS to achieve sensitivity to magnetic forces. To ensure accurate temperature readings in the $T = 9$–13 K regime, the temperature of the AFM sample stage was calibrated by means of a niobium wire with a superconducting temperature of $T_{\mathrm{C}} = 9.25$ K placed on the AFM sample stage. Correspondingly, we expect that the difference between the nominal temperature and the actual sample temperature is well below 1 K.

In nc-AFM mode the frequency f of an oscillating cantilever is measured via a phase-locked loop and kept constant by the topography feedback loop. The frequency shift Δf with respect to the resonance frequency f_0 far away from the sample provides a measure of the force gradient apparent between tip and sample. In addition, the oscillation amplitude A is kept constant by adjusting the excitation amplitude A_{exc}. Electrostatic interactions between tip and sample have been minimized using an additional FM-Kelvin control loop without any further lateral information in the measured contact potential difference.

We could not obtain magnetic contrast in magnetic force microscopy mode, where the tip is retracted from the surface and the conservative magnetic forces are measured by means of the induced frequency shift Δf. Instead, a dissipative force interaction induced the magnetic contrast in the excitation channel when the tip was brought close to the sample surface. The nature of this dissipative interaction is subject to further investigations.

With knowledge of the cantilever's spring constant k, the actual oscillation amplitude A, the resonance frequency f, the effective quality factor $Q_{\mathrm{eff},0}$ and the signal-to-drive ratio R_0 far away from the sample, we compute the dissipated power from the measured excitation amplitude as

$$P = \frac{\pi k f R_0 A}{Q_{\mathrm{eff},0}} \cdot A_{\mathrm{exc}}$$

For the images in Fig. 2 these parameters are $k = 3.4\ \mathrm{N\,m^{-1}}$, $A = 3$ nm, $Q_{\mathrm{eff},0} = 4.28 \times 10^5$, $f = 70.87$ kHz, $R_0 = 30.92\ \mu\mathrm{m\,V^{-1}}$ with excitation amplitudes ranging from 150 μV to 1.1 mV.

Small-angle neutron scattering. Small-angle neutron scattering (SANS) was used to study the long-wavelength, microscopic magnetic states in a 25.5 mg single crystal sample of GaV_4S_8. The SANS measurements were carried out using the D33 instrument at the Institut Laue-Langevin (ILL), Grenoble, France, and the SANS-II instrument at the Swiss Spallation Neutron Source (SINQ), Paul Scherrer Institut, Switzerland. In a typical instrument configuration, neutrons of wavelength 5 Å were selected with a full-width at half-maximum (FWHM) spread ($\Delta\lambda/\lambda$) of 10%, and collimated over a distance of 5.3 m before the sample. The scattered neutrons were collected by a two-dimensional multi-detector placed 5 m behind the sample.

The single-crystal sample of GaV_4S_8 was mounted inside a horizontal field cryomagnet that was installed on the beamline so that the direction of applied magnetic field was approximately parallel to the neutron beam. The sample was oriented to have a horizontal scattering plane that included the [100] and [111] crystal directions. Applying the magnetic field along either of these directions was achieved simply by rotating the sample stick inside the cryomagnet. The SANS measurements were done by both tilting and rotating the sample and cryomagnet together through angular ranges (rocking angles) that moved the magnetic diffraction peaks through the Ewald sphere. The SANS patterns presented in Fig. 4 were constructed by summing together the detector measurements taken at each rocking angle, which allows all of the Bragg spots to be presented in a single image.

For the data shown in Figs 4 and 5, the FWHM q-resolution within the plane of the SANS detector was $\Delta q_r = 0.006\ \mathrm{Å^{-1}}$ parallel to the scattering vector, and $\Delta q_t = 0.005\ \mathrm{Å^{-1}}$ in the perpendicular direction. In this plane all individually resolved Bragg peaks were resolution-limited. In contrast, the rocking curves, which probe the magnetic correlations perpendicular to the detector plane, are not resolution-limited; for the data shown in Fig. 5a the FWHM angular resolution is about 0.1°. This demonstrates that in general for our measurements the rocking curve widths are always dominated by the magnetic mosaicity.

The form of the rocking curves at low field, a central peak on top of a flat and finite component (Fig. 5a), arises because the overall scattering receives contributions from both the unique domain with easy axis along the field (the central peak), and a different rhombohedral domain (flat component). As evidenced in the rocking curve measurements, the Bragg peaks due to the scattering from each type of domain have clearly different shapes in the longitudinal direction perpendicular to the detector plane. We use this observation to extract estimates for the different correlation lengths along (central peak) and perpendicular to the vortex cores (flat component) of the SkL states. From the width of the central peak we estimate the correlation length along the vortex cores to be $\xi_{\parallel} \approx 540$ nm, according to $\xi_{\parallel} \approx 2\pi/(|\mathbf{q}|\sin(\varphi))$, where φ is the FWHM of the central peak in the rocking curve in radians. The explored angular range of the rocking curves only allows an upper estimate of $\xi_{\perp} \leq 110$ nm for the correlation length perpendicular to the vortices.

Theoretical calculations. The Monte Carlo calculations for Fig. 6 are performed for the model in equation (1) on a two-dimensional triangular lattice with 144×144 sites and periodic boundary conditions. The XXZ-type anisotropy in the exchange term comes from the orbital ordering with $3z^2 - r^2$-type orbitals pointing in the [111] direction, taken as the z axis in the calculation[26]. The ratio of $J_{\parallel}/J_{\perp}$ was determined from a mean-field analysis of the low-temperature magnetization curves, with the value of $D/J_{\perp}$ fixed according to the observed cycloidal pitch, a_{cyc}.